International Journal of Geo-Information

MDPI

Article

Identification and Mapping of Soil Erosion Processes Using the Visual Interpretation of LiDAR Imagery

Petra Đomlija [1], Sanja Bernat Gazibara [2], Željko Arbanas [1] and Snježana Mihalić Arbanas [2,*]

[1] Faculty of Civil Engineering, University of Rijeka, 51000 Rijeka, Croatia; petra.domlija@gradri.uniri.hr (P.Đ.); zeljko.arbanas@gradri.uniri.hr (Ž.A.)

[2] Faculty of Mining, Geology and Petroleum Engineering, University of Zagreb, 10000 Zagreb, Croatia; sbernat@rgn.hr

* Correspondence: smihalic@rgn.hr; Tel.: +385-01-5535-765

Received: 26 July 2019; Accepted: 29 September 2019; Published: 7 October 2019

Abstract: Soil erosion processes are a type of geological hazard. They cause soil loss and sediment production, landscape dissection, and economic damage, which can, in the long term, result in land abandonment. Thus, identification of soil erosion processes is necessary for sustainable land management in an area. This study presents the potential of visual interpretation of high resolution LiDAR (light detection and ranging) imagery for direct and unambiguous identification and mapping of soil erosion processes, which was tested in the study area of the Vinodol Valley (64.57 km^2), in Croatia. Eight LiDAR images were derived from the 1 m airborne LiDAR DTM (Digital Terrain Model) and were used to identify and map gully erosion, sheet erosion, and the combined effect of rill and sheet erosion, with the ultimate purpose to create a historical erosion inventory. The two-step procedure in a visual interpretation of LiDAR imagery was performed: preliminary and detailed. In the preliminary step, possibilities and limitations for unambiguous identification of the soil erosion processes were determined for representative portions of the study area, and the exclusive criteria for the accurate and precise manual delineation of different types of erosion phenomena were established. In the detailed step, the findings from the preliminary step were used to map the soil erosion phenomena in the entire studied area. Results determined the highest potential for direct identification and mapping of the gully erosion phenomena. A total of 236 gullies were identified and precisely delineated, although most of them were previously unknown, due to the lack of previous investigations on soil erosion processes in the study area. On the other hand, the used method was proven to be inapplicable for direct identification and accurate mapping of the sheet erosion. Sheet erosion, however, could have been indirectly identified on certain LiDAR imagery, based on recognition of colluvial deposits accumulated at the foot of the eroded slopes. Furthermore, the findings of this study present which of the used LiDAR imagery, and what features of the imagery used, are most effective for identification and mapping of different types of erosion processes.

Keywords: soil erosion; recognition features; visual interpretation; delineation; LiDAR DTM; topographic derivatives; erosion inventory; Vinodol Valley

1. Introduction

Soil erosion is one of the major causes of land degradation [1]. It refers to processes of removal of near-surface material from hillslope by running water [2]. Starting with rainfall, the evenly distributed runoff leads to sheet erosion. A concentration of flow results in the formation of rills, which often develop into gullies. Gully erosion is considered to be one of the processes that greatly contribute to landscape formation [3,4], generally causing its degradation [5–8]. Soil losses and sediment production,

economic impacts on elements of infrastructure, and overall landscape dissection have significant influence on human activities, and vice versa, and can result in land abandonment. Therefore, soil erosion is a type of geological hazard [9,10].

Identification of areas affected by the soil erosion is necessary for sustainable land management [3,8,11]. Furthermore, any kind of susceptibility, hazard, and risk assessment requires the knowledge of the type and the spatial distribution of hazardous phenomena [12]. Thus, an accurate mapping of the topographic signatures specific for geological hazards represents an important and first step in the preparation of geomorphological inventories e.g., [13,14]. For this purpose, the application of remote sensing technologies has been widely confirmed as practical and effective [10]. Among these technologies, the airborne light detection and ranging (LiDAR) provides the generation of high quality digital terrain models (DTM), which have been so far effectively used in a variety of terrain analyses.

Within the natural hazard studies based on the applications of airborne LiDAR data, studies on landslides have made the greatest advances [10,15,16]. One of the most powerful methods used for landslide mapping and preparation of landslide inventories is the visual interpretation of high resolution (HR) LiDAR imagery [14]. This method is based on visual recognition and manual delineation of morphological features by experts, using different types of visualizations of LiDAR data in the form of HR imagery describing the terrain [17–24]. Different types of LiDAR imagery (i.e., LiDAR maps) can be easily derived from the bare-earth DTM [14] created from the point cloud data acquired by airborne laser scanning (ALS) [25–27]. The effectiveness of the method of visual interpretation of airborne LiDAR imagery has also been confirmed by geomorphological identification and mapping of glacial landforms [28,29], river valley environments [30], and erosional glaciotectonic landforms [31]. Cavalli and Marchi [32] performed an analysis of the surface morphology of an individual alluvial fan. Notebaert et al. [33] tested the possibilities for mapping of channel patterns, colluvial hillslopes, and fan deposits. Analysis of airborne LiDAR imagery has also been successfully used for identification and mapping of superficial deposits [34], logjams [35], and late Quaternary glacial lake floods [36]. Within most of the visual analyses, the hillshade map has been commonly used as the basic map e.g., [21,23,37], in some cases as the only map used [31,38], but it has been mostly visually analyzed in combination with the slope map and the contour line map e.g., [23], the curvature maps e.g., [22], and the topographic roughness map e.g., [39].

The literature review reveals that a few studies have used the method of visual interpretation of LiDAR imagery for identification and mapping of the soil erosion processes, mainly focusing on mapping gullies. James et al. [40] tested the ability of the 2–4 m airborne LiDAR DTM to map gullies for two gully systems under thick forest canopy by using only the contour line map. Although the results of gully mapping were a major improvement over the previously available topographic maps, the study provided a low mapping accuracy due to the fact that certain closely spaced small gullies were omitted from the gully maps. Authors noted that a possible reason for that fact could be the spatial resolution of the DTM that was used. Manual delineation of linear gully elements or gully polygons was performed within certain research, primarily for the verification of results obtained using the automatic methods for gully detection. Evans and Lindsay [11] demonstrated that the planform gully pattern was accurately represented in an automated approach to gully extraction at the landscape scale in upland peatlands from the 2 m airborne LiDAR DTM. Hofle et al. [41] performed an automatic detection and delineation of gullies in cushion peatlands from a 0.5 m terrestrial LiDAR DTM, and for the results verification they used a hillshade map. A curvature map that combines both the profile and the planform curvature, derived from the 1 m airborne LiDAR DTM, was used to map and quantify the gullies initiated by the military training activities [42]. Airborne LiDAR curvature-based approaches for a semi-automated recognition of gullies were also proposed by Baruch and Filin [43], as well as Korzeniowska and Korup [44].

Conventional field methods e.g., [4,45] and the visual analysis of aerial photography e.g., [46, 47] have also been widely used for mapping gullies. However, the determination of gully geometry in the field is often difficult [48], as well as impractical in areas of extensive gully networks [11], while the

analysis of aerial photography is significantly less effective in areas under forest canopies e.g., [40]. Several gully susceptibility analyses have been performed by using the gully inventory maps as input parameters, which were prepared based on the visual interpretation of aerial photographs coupled with field surveys [3], or using only the multiple detailed field investigation data [8,49]. Mapping of gullies was also carried out based on the visual interpretation of HR satellite images e.g., [50–52], even at national scale [53].

To the authors' knowledge, there are no published papers that, in detail, describe the procedure of visual interpretation of HR LiDAR imagery as the method to identify and map different types of soil erosion processes, with the ultimate objective of developing a historical erosion inventory. The main objective of this study was to assess the potential of eight different LiDAR images, derived from the 1 m airborne LiDAR DTM of the Vinodol Valley (64.57 km^2) in Croatia, to identify and map gully erosion, sheet erosion, and combined effect of rill and sheet erosion from the LiDAR imagery directly. The study area is mostly composed of flysch rock mass [54] covered with various types of superficial deposits [55], and it is specifically known for hazardous processes, particularly soil erosion [56–58]. In this study, a two-step procedure of visual interpretation of LiDAR imagery was performed: preliminary and detailed. In the preliminary step, a representative portion of the study area was chosen with the main aims to: (1) determine the possibilities and limitations of a direct and unambiguous identification of different types of soil erosion processes, and (2) establish the exclusive criteria for mapping gully, combined, and sheet erosion. In the detailed step, the findings from the preliminary step were used to map the soil erosion phenomena in the entire study area. In this paper, characteristic examples of identification and mapping of different types of erosion phenomena, in particular the gully erosion phenomena, are presented and described in detail. The findings of this study inform which LiDAR maps are the most effective in providing geomorphological clues and which erosion processes can be identified and recorded with a high geographical and thematic accuracy using the datasets and proposed procedures, which can be used as guidance in future studies on erosion mapping in similar study areas.

2. Materials

2.1. Study Area

The procedure taken to identify and map the soil erosion processes has been developed for the Vinodol Valley (64.57 km^2), which is situated in the northwestern coastal part of the Republic of Croatia (Figure 1). The area is predominantly rural, and it has been inhabited since the prehistoric times [59]. More than 50 small settlements situated in the valley are connected by a relatively dense road network consisting of two county roads, several local roads, and numerous unnamed roads and pathways. Prevailing elevations are in the range between 100 and 200 m a.s.l., with an average elevation of 283 m a.s.l. [55]. Slope angles between 5° and 20° prevail, and the average angle is 16°. The valley has an irregular, elongated shape. The steep valley flanks are built of Upper Cretaceous and Paleogene carbonate rocks, while the lower parts and the bottom of the valley are built of Paleogene flysch rock mass [54]. Flysch bedrock is almost entirely covered by Quaternary eluvial, colluvial, and proluvial soils [55], which are formed by geomorphological processes active both in the carbonate and flysch rock mass [58,60]. The climate is maritime [61], with mean annual precipitation between 300 and 700 mm. The rainy period lasts from November to May, with precipitation at its maximum in November when rainstorms of high erosive potential frequently occur. Forests cover an area of 32.19 km^2 [62]. Other important land covers are shrubs (6.17 km^2) and natural pastures (5.66 km^2). The topography of the Vinodol Valley has been generally divided into three parts, i.e., the northwestern, the central and the southeastern parts [60]. The northwestern and the central parts belong to the Dubračina River Basin, while the southeastern part belongs to the Suha Ričina River Basin.

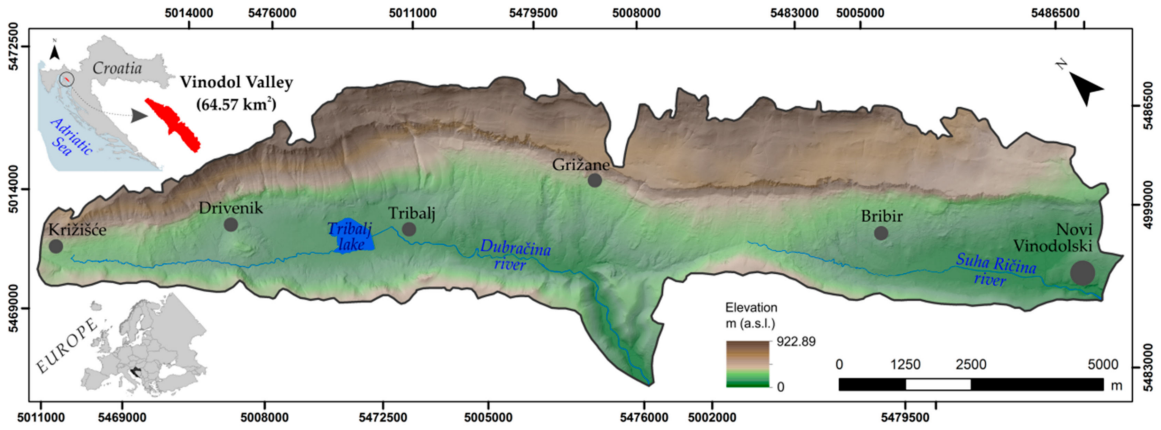

Figure 1. Geographical location and the relief map of the Vinodol Valley.

Past and current erosion processes have significantly influenced the overall topography and land degradation in the Vinodol Valley [55]. Erosion processes, mainly associated with landslides, cause direct damage on public and private properties [63]. Numerous gullies, varying in size and shape, have been formed along the surface of poorly maintained roads and pathways (Figure 2a–c), private properties, and agricultural terraces (Figure 2d,e), or along their boundaries (Figure 2f). In some gullies, attempts have been made to control the erosion by way of stone check dams (Figure 2g). Many gullies have been developed in forested areas (Figure 2h). Most of them are difficult to approach due to the relief conditions and the land cover. An unusually intense erosion is specific to the relatively large gully of the Slani Potok (''Salty Creek''), situated in the central part of the Vinodol Valley (Figure 2i). Badlands have been formed in its upper part, associated with shallow landslides (Figure 2j). The area of the Slani Potok represents a unique phenomenon within the Dinaric flysch [57] and so far it has been given the most attention during previous investigations [56,63–65].

Superficial deposits and flysch outcrops have also been affected by associated action of rill and sheet erosion [55]. The combination of these processes can be recognized in the field by way of a small drainage network, associated with sediments transported by the sheet wash (Figure 2k,l). In such small drainage networks, rills are being formed at the head of the concave drainage systems (Figure 2m). For the purpose of this study, these interrelated erosion processes were designated by the term of combined erosion. In the Vinodol Valley, the combined erosion phenomena mostly occurs within the relief concavities covered by sparse vegetation, along the surface of which the convergence of the running water increases the erosion potential [66]. Sheet erosion can be recognized in the field predominantly on the surface of eluvial deposits (Figure 2n). It is also active in some forest areas during the autumn and winter periods (Figure 2o), as it is evidenced by the exposed tree roots (Figure 2p).

However, despite the fact that soil erosion processes are a common geological hazard in the Vinodol Valley e.g., [65], and that the influence of these processes on the landscape is well known since the beginning of the last century [59], there are no previous studies in this area that are particularly focused on soil erosion. Therefore, any kind of older research data of about the identification or mapping of the soil erosion phenomena were not available.

Figure 2. Photographs of erosion phenomena identified in the Vinodol Valley. The gully erosion phenomena formed along: (**a**) the local road, (**b**,**c**) pathways, (**d**,**e**) agricultural terraces, and (**f**) their boundaries; (**g**) an example of the stone check dam built to control the gully erosion; (**h**) a gully formed under the forest; (**i**) a view from the air of the central part of the Vinodol Valley, with depicted detail of the Slani Potok gully, shown in (**j**). (**k**–**m**) The combined erosion phenomena characterized by the small drainage network associated with colluvial deposits; (**n**) the sheet erosion phenomena formed in eluvial deposits, and in (**o**) the forest, as indicated by the exposed tree roots (**p**).

Apart from the soil erosion, traces of past and recent human activities (i.e., agricultural terraces, roads, pathways), as well as the topographic signatures of diverse geological materials, are present along the surface of almost the entire study area, and they are clearly expressed on the LiDAR imagery (Figure 3a). Most of the agricultural terraces, which were built in the historical time along the flysch slopes for vineyards [59], are currently abandoned and covered by dense forests (Figure 3b).

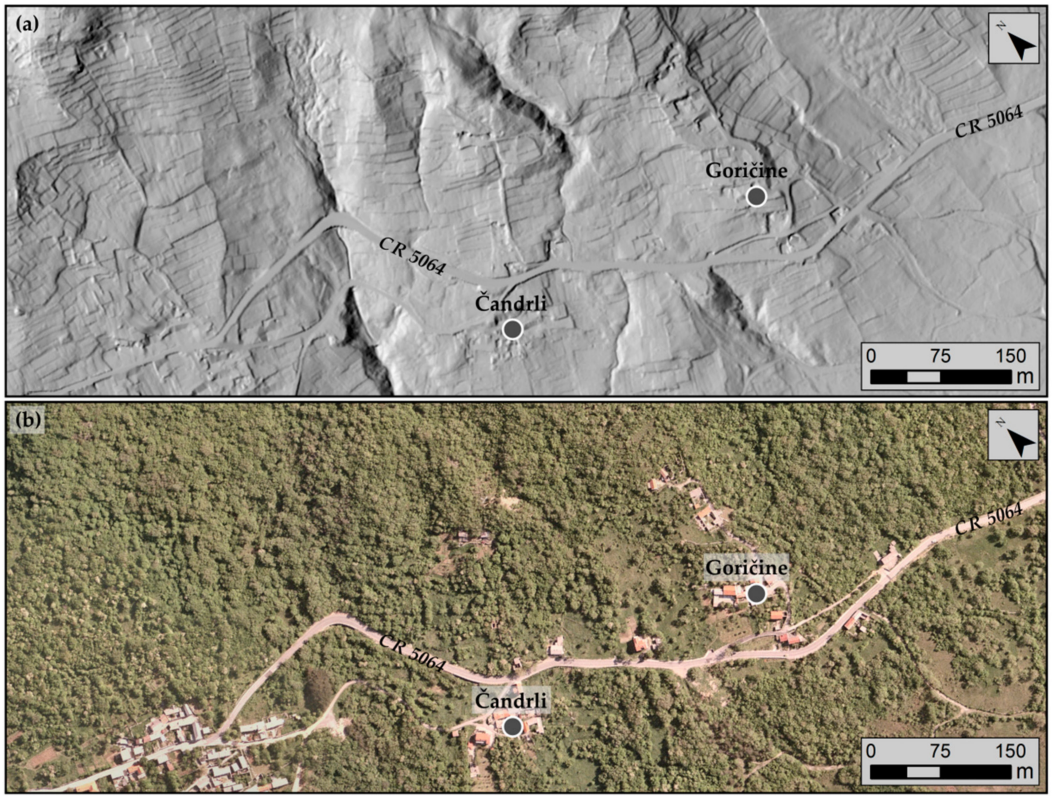

Figure 3. A representative example of topography of the Vinodol Valley shown on: (**a**) the semi-transparent (50%) hillshade map 45°/45° over the hillshade map 315°/45°; and (**b**) the digital orthophoto map 1:5000.

2.2. High Resolution LiDAR data

The LiDAR data used in this study were acquired in March 2012, which corresponds to the leaf-off period in Croatia. Airborne laser scanning was performed in nine flight lines from two directions with azimuth angles of 315°and 135°, by using the multi-return LiDAR system. Point measurements were post-processed by filtering into returns from all objects and vegetation, and into returns from the bare ground. Bare-ground returns were acquired at the point density of 4.03 points per square meter, with an average point distance of 0.498 meters. They were used for the creation of the bare-earth DTM with a 1 × 1 m resolution, by using a triangulated irregular network interpolation. The average accuracy of the altitude data is 30 cm, but it may be smaller in areas covered by dense forests.

For the visual analysis of topography, eight types of imagery were derived from HR LiDAR DTM using the standard tools in the computer software *ArcGIS 10*. Three hillshade maps were created with the Hillshade tool, using azimuth angles of 315° and 45°, and sun angles of 45° and 30°. No vertical exaggeration was used. In order to obtain the optimal shaded relief for each part of the study area [38,67], hillshade maps were additionally overlapped in two combinations: (a) the semi-transparent (50%) hillshade map 45°/45° over the hillshade map 315°/45°, and (b) the semi-transparent (50%) hillshade map 45°/30° over the hillshade map 315°/45°. The slope map was generated with the standard Slope tool, and then it was reclassified according to classification established by [68]. On the slope map, areas of higher slope angles are displayed in red and orange, while areas of lower slope angles are displayed in light and dark green. The contour line maps with 1 m and 2 m contour intervals were created by using the standard Contour tool. The topographic roughness map was calculated according to the slope variability methode.g., [69,70], where the slope variability implies a difference between the minimum slope angle and the maximum slope angle in the selected area. The input parameter for the creation of the topographic roughness map was the slope map. Using the Focal Statistics tool, the maximum slope angle raster (S_{max}) and the minimum slope angle raster (S_{min}) were generated.

Slope variability (SV), i.e., the topographic roughness map, was then calculated by using the Raster Calculator, as:

$$SV = S_{max} - S_{min}. \quad (1)$$

The continuous color ramp was used for the visualization of data on the topographic roughness map. Areas of high topographic roughness are shown in brown, orange, and yellow, while the areas of low topographic roughness are shown in blue and purple. The aspect map was derived from the LiDAR data by using the standard Aspect tool, and it was reclassified into the aspect classes defined by sides of the world [71]. The profile curvature map and the planform curvature map were calculated by using the Curvature tool. In the profile curvature map, concave slopes are shown in blue, while the convex slopes are shown in red. In the planform curvature map, convex slopes are shown in blue, while the concave slopes are shown in red. The input parameters for the creation of the stream power index map were the slope map and the flow accumulation map. The stream power index map was calculated by using the Raster Calculator, according to [72] as:

$$SPI = \ln(flow\ accumulation) \times \left(\frac{slope}{100}\right). \quad (2)$$

The continuous color ramp was used for the visualization of data on the stream power index map. The lines with the highest values of the stream power index are shown in white, while the lines with the lowest values of the stream power index are shown in black.

2.3. Other Topographic and Lithologic Data

Additional topographic information that was used in this study was available from two official state maps: the Croatian base map (CBM) 1:5000, and the digital orthophoto map (DOM) 1:5000, which was created in 2006. Lithologic data were available from the engineering geological map (EGM) of the Vinodol Valley on the scale of 1:5000 [55], which was created based on the detailed visual interpretation of HR LiDAR imagery from March 2012.

3. Methodology for Preparation of Erosion Inventory

A general overview of methodology for the preparation of erosion inventory for the case study of Vinodol Valley is presented by a flowchart in Figure 4. The methodology was primarily based on the analysis of HR LiDAR imagery, which was performed in two steps: the preliminary and the detailed visual interpretation. The procedures of the visual interpretation of LiDAR imagery were complemented by the field investigations data, as well as the analysis of additional topographic (CBM 1:5000; DOM 1:5000) and lithologic (EGM 1:5000) data.

3.1. Preliminary Visual Interpretation of HR LiDAR Imagery

The preliminary visual interpretation of HR LiDAR imagery was the first step in the preparation of the erosion inventory. This procedure was carried out for one portion in each part of the Vinodol Valley, which was evaluated as representative of diversity of the soil erosion processes, based on the visual analysis of the hillshade map and reconnaissance geomorphological mapping. The main aims of the preliminary visual interpretation of HR LiDAR imagery were (Figure 4): (a) determination of possibilities for unambiguous identification and mapping of the erosion processes directly from the HR LiDAR imagery; and (b) the definition of criteria for identification and mapping of the erosion phenomena. For this purpose, an iterative visual inspection of eight LiDAR maps and their combinations was carried out at on a scale between 1:500 and 1:5000, depending on the type, shape, and size of the erosion phenomena. In this step, eight LiDAR maps were intermittently analyzed, individually or combined, through repeated rounds of visual interpretation with the main objective being to determine which individual map or which combination of maps best reflected a particular morphological feature. This analysis was carried out simultaneously with field investigations (Figure 4).

The verification of preliminary remote sensing results was conducted during the winter and the early spring months in 2015 and 2016, due to the sparse and leaf-off vegetation. For the multiple field checks, the hillshade map and the DOM 1:5000 with mapped boundaries of identified erosion phenomena were prepared. Although field investigations were partially limited due to the complex morphological features and land cover conditions in the studied area, it was possible to check at least a small portion of each erosion phenomenon identified on LiDAR imagery. On the other hand, certain erosion phenomena were first identified in the field, prior to the LiDAR imagery, and their on-site locations were subsequently visually analyzed and identified on LiDAR maps. Such an iterative approach, which combined the visual interpretation of LiDAR imagery and field investigations, has shown that all topographic signatures of the erosion processes in the Vinodol Valley cannot be equally recognized on LiDAR imagery. Thus, it was necessary to analyze other available topographic and lithological data (Figure 4), which provided additional helpful information indicative of the soil erosion processes, for example, information about the spatial distribution of superficial deposits accumulated at the foot of the flysch slopes after removal by running water, the land cover alterations, as well as information about the spatial distribution of drainage system elements and elements of man-made structures, which were confirmed to have been affected by the soil erosion. The procedure of the preliminary visual interpretation of HR LiDAR imagery was complex, iterative, and thus, lengthy. However, it was necessary to perform it in the earliest phase of the investigation in order to avoid any possible geomorphological misinterpretations and to obtain the greatest possible degree of geographical accuracy and thematic certainty of the remote sensing results during the detailed visual interpretation of HR LiDAR imagery.

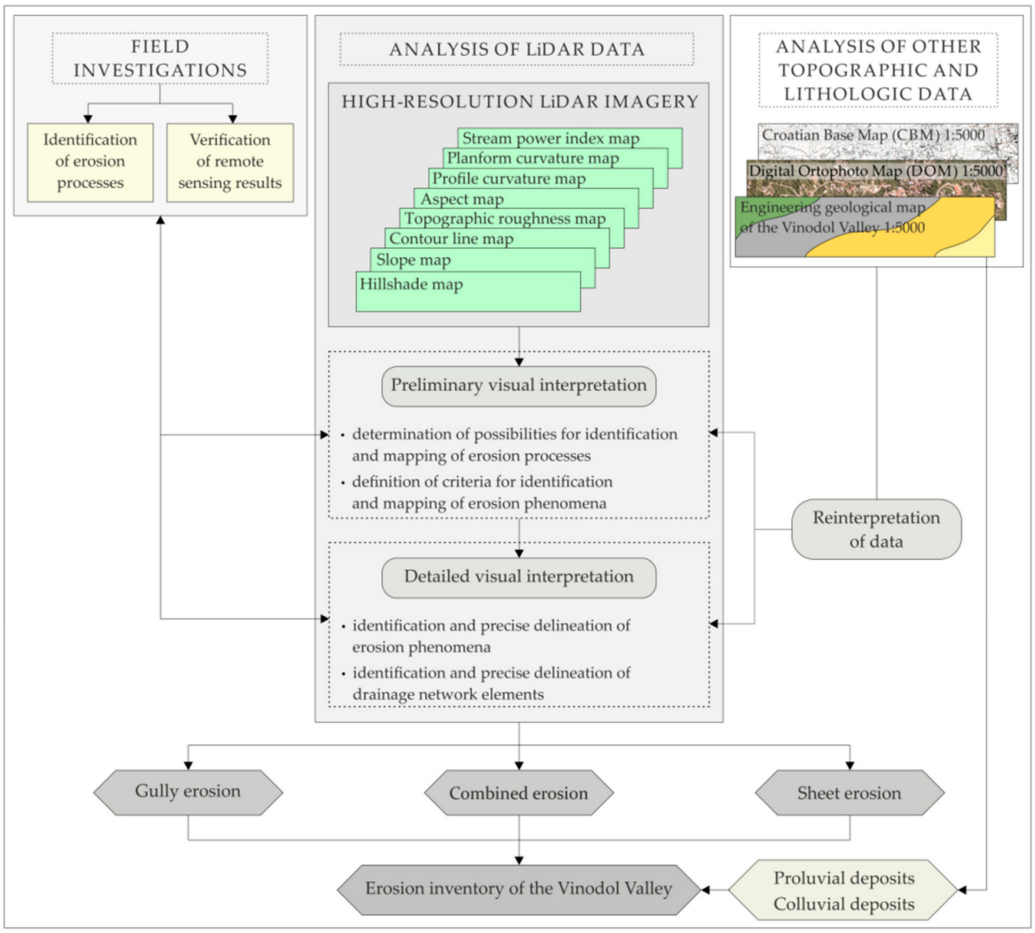

Figure 4. Flowchart of the methodology for the preparation of the erosion inventory.

3.2. Criteria for Identification and Mapping of Erosion Phenomena

Erosion phenomena formed at the surface affected by the erosion processes can, in most cases, be recognized on LiDAR imagery by specific topographic signatures [16]. In this study, several morphological and lithological features, indicative of erosion processes, were visually analyzed on different LiDAR maps. These recognition features can be divided into two groups. The first group of recognition features allows direct identification and mapping of the erosion phenomena from HR LiDAR imagery (i.e., direct recognition features), including: (a) shape, (b) appearance, (c) size, (d) texture, and (e) morphometric characteristics. For example, shape is the most useful recognition feature for unambiguous identification of the gully erosion processes, because they form gully channels on the affected surface [2]. Morphometric characteristics are also useful for recognition of the gully channel due to abrupt changes of slope angle and aspect between the gully channel walls and the surrounding slopes. The second group of recognition features enables indirect identification and mapping of the erosion phenomena from HR LiDAR imagery (i.e., indirect recognition features), including: (a) accumulations of eroded sediment, i.e., colluvial deposits and proluvial deposits from flysch [55]; (b) erodible material, i.e., eluvial deposits with flysch outcrops [55]; (c) topographic location; (d) pattern; and (e) man-made structures. For example, an area affected by the sheet erosion processes can be indirectly recognized based on the recognition of the colluvial deposits that have been formed by the sheet wash along the surface of erodible slopes. The pattern, for example, can be an important recognition feature for identification of the combined erosion processes due to the formation of gullies in central parts of relief concavities affected by the convergence of running water [66].

Criteria for identification and mapping of the soil erosion phenomena are listed in Table 1. The criteria represent characteristic sets of direct and indirect recognition features indicative of soil erosion processes coupled with HR LiDAR maps and other data, which are considered as the most effective for identification and mapping, based on the preliminary visual interpretation of HR LiDAR imagery.

3.3. Detailed Visual Interpretation of HR LiDAR Imagery

The detailed visual interpretation of HR LiDAR imagery implies identification and precise delineation of individual erosion phenomena in the whole study area (Figure 4) based on the established criteria (Table 1). By that, the precise delineation implies the procedure of manual drawing of polygons and lines, such that provides the highest level of geographical accuracy given the 1 m DTM resolution, which was performed by one and the same expert.

The precise delineation of gully channels wider than three meters was performed using polygons. For each gully, thalwegs were also precisely delineated using lines. The precise delineation of gully channels narrower than three meters was performed using lines that, in these cases, represent the gully thalwegs. During this procedure, the gully width was manually measured on the slope map along the imaginary line with ends located at the points of the distinct change of slope angle [48], in the part of a channel which was visually evaluated as the part of the smallest width. The three meter threshold for mapping gullies, whether using polygons or lines, was chosen for two main reasons: (a) because the gullies narrower than three meters occupy only two or three pixels; and (b) for the purpose of an optimal adjustment of the quality of results to the final scale of 1:5000 for preparation of the erosion inventory map. For additional checks during the mapping, the CBM 1:5000 was also visually inspected, mainly for the reason that it shows the paths of the occasional concentrated runoff, as well as the pathways and forest roads.

Table 1. Criteria for identification and mapping of soil erosion phenomena.

Soil Erosion		Indicative Recognition Feature		LiDAR and Other Data Most Effective for Identification and Mapping
Gully erosion	direct	Shape	Elongated or branchy shape of gully channel	Hillshade map Slope map Aspect map
			Linear shape of gully thalweg	Stream power index map Planform curvature map Profile curvature map
		Morphometric characteristics	Change in slope angle between gully channel and surrounding slopes Change in aspect between gully channel and surrounding slopes	Slope map Aspect map
		Texture	Rough surface within gully channel	Topographic roughness map
	indirect	Accumulations of eroded sediment	Proluvial deposits, fan-shaped	Contour line map Topographic roughness map EGM 1:5000
		Pattern	Proluvial deposits situated at the mouth of gully channel	
		Man-made structures	Gully formation along pathways and boundaries between agricultural terraces	Slope map Planform curvature map CBM 1:5000
Combined erosion	direct	Appearance Size Texture	Disturbed slope surface appearance Small sized drainage network Rough slope surface	Hillshade map Stream power index map Topographic roughness map
	indirect	Topographic location	Relief concavities	Aspect map Contour line map Slope map
		Pattern	Gullies formed in the central part of relief concavities	Delineated gully phenomena
		Accumulations of eroded sediment	Proluvial deposits and colluvial deposits	Contour line map Topographic roughness map EGM 1:5000
Sheet erosion	direct	Texture	Smooth surface of the affected area	Topographic roughness map
	indirect	Erodible deposits	Eluvial deposits with flysch outcrops	EGM 1:5000
		Accumulations of eroded sediment	Colluvial deposits	

The precise delineation of the combined erosion phenomena was performed after the mapping of gully erosion phenomena was carried out, since the gullies formed in the central part of relief concavities were one of the criteria for identification of combined erosion (Table 1). The mapping was also performed using polygons, depicting the whole areas affected by the combined erosion processes. Recognition of the combined erosion phenomena (Table 1) was performed on a scale ranging from 1:1000 to 1:5000. The precise delineation of polygons was carried out on a scale mostly larger than 1:1000. As in the case of mapping the gullies, a high level of precision in mapping of the combined erosion phenomena was achieved by drawing the separate portions of polygons based on the visual analysis of different LiDAR maps, and subsequent merging of drawn lines into a unique polygon using the tools in ArcGIS.

The mapping of the sheet erosion phenomena was carried out last, after completing the mapping of the gully and the combined erosion phenomena. It was mainly based on the reinterpretation of lithologic data available from the engineering geological map of the Vinodol Valley [55]. The delineation was performed using polygons, depicting the whole areas affected by the sheet erosion processes.

The detailed visual interpretation of HR LiDAR imagery was carried out simultaneously with the field verifications of remote sensing results (Figure 4), which was carried out by filed walks. Verification of the results was conducted on a particular number of all types of soil erosion, especially gullies because many of these phenomena form in the vicinity of roads and along pathways (Figure 2), conducting a comparison of visual interpretation data and field mapping of erosion occurrences. In all checked examples there was a high accuracy of compared data. However, field checks were not possible for all delineated erosion phenomena, due to the size of the study area and difficulties in accessing unreachable terrain parts.

4. Results of Detailed Visual Interpretation of HR LiDAR Imagery

4.1. Identification and Mapping of Gully Erosion Phenomena

An example of identification and mapping of two linear and relatively large gullies of well-preserved topography, formed in the urbanized area in the central part of the Vinodol Valley, is presented in Figure 5. Both gully channels have an elongated shape and a non-uniform width. The larger gully (area of 5.45 ha) is marked with number 1 in Figure 5a, and the smaller gully (area of 3.46 ha) is marked with number 2. The shapes of both gully channels and thalwegs were firstly and easily recognized on the hillshade map (Figure 5a). The narrowing of gully channels in the area above the county road (CR 5064) is also recognizable in the hillshade map. The aspect map generally reflects the shape of both gully channels due to the opposite aspects of channel walls, as well as due to the changes of aspect between the gully channels and the surrounding slopes. However, the aspect map overestimates the width of the smaller gully in the part of the gully where only the thalweg is formed (pointed out with white arrows in Figure 5b). The shape and the boundary of the larger gully channel can be most easily recognized on the slope map (Figure 5c), given the distinct changes in slope angle between the gully channel and its surroundings. The visual interpretation of the slope map was, therefore, sufficient for a precise delineation of almost the entire boundary of the larger gully channel. Only small portions of the right channel walls in its middle and lower parts were precisely delineated based on the visual interpretation of the aspect map (Figure 5b). A steep topography of the left channel wall of the smaller gully can also be easily recognized on the slope map (Figure 5c), as well as its branching along the pathway passing between agricultural terraces (pointed out with blue arrows in Figure 5c). On the other hand, the boundary of the right channel wall of the smaller gully is not so distinctly marked on the slope map (Figure 5c). Still, it was possible to track it on the slope map along the endings of the agricultural terraces and separately map it in combination with the visual interpretation of the aspect map (Figure 5b). The stream power index map (Figure 5d) and the profile curvature map (Figure 5e) have provided a precise delineation of the main gully thalwegs and its branches, both within and out of the gully channels. This map has also allowed for the recognition

of almost the entire boundary of the larger gully channel, given the clearly expressed slope ridges. Final delineated polygons representing the gully channels and lines representing the gully thalwegs are presented on the hillshade map in Figure 5f. Both identified gullies were previously known before the LiDAR data became available. However, their full extent and the exact shape were not possible to determine prior this study because the whole area is covered with dense forest (Figure 5g). The erosion processes could only be assumed by way of the alteration in the type of vegetation cover, visible on DOM 1:5000. Additionally, the analysis of the CBM 1:5000 helped in identification of the gully erosion process along the pathway passing between agricultural terraces, as highlighted with red arrows in Figure 5h.

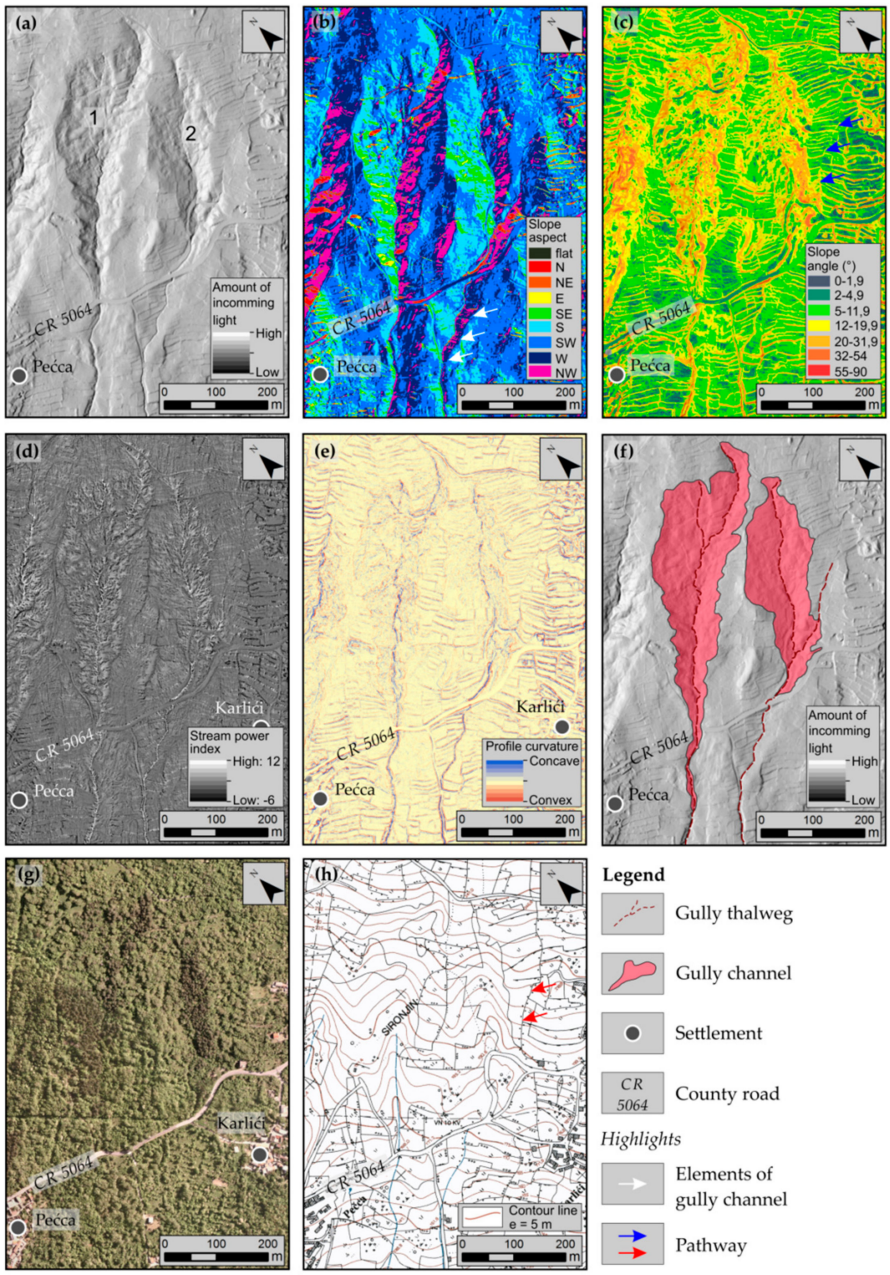

Figure 5. Visualization of topography of two linear gullies of well-preserved topography on high resolution (HR) light detection and ranging (LiDAR) imagery: (**a**) the hillshade map 315°/45°; (**b**) the aspect map; (**c**) the slope map; (**d**) the stream power index map; and (**e**) the profile curvature map. (**f**) The hillshade map with delineated polygons representing the gully channels and lines representing the gully thalwegs; (**g**) the DOM 1:5000; and (**h**) the CBM 1:5000 of the interpreted area.

An example of identification and mapping of the gully with a more complex shape is shown in Figure 6. The gully (2.58 ha) has been formed within the urbanized area in the northwestern part of the Vinodol Valley. Only the shape of the left channel wall can be recognized on the hillshade map (Figure 6a) and on the slope map (Figure 6b). The shape of the right channel wall could only be recognized on the slope map overlapping with a contour line map with 1 m contour interval (outlined with blue arrows in Figure 6b). Still, its accurate recognition was difficult, given the frequent changes of slope angle in the area surrounding the gully. The linear features of gully channel along its left border are also clearly expressed on the aspect map (Figure 6c). However, this map was almost entirely ineffective for the analysis of topography within the right channel wall because of too frequent changes of slope aspect. The topographic roughness map (Figure 6d) clearly reflects the rough surface within the gully channel, especially in its central part. However, the texture within the gully is similar to its surroundings, whose high roughness is due to the presence of other gullies formed in the vicinity (depicted with red and white polylines) and the presence of debris material (depicted with black and white polyline) originating from the weathering of limestone situated at the hypsometrically higher slopes [55].

By contrast, the planform curvature map (Figure 6e), and the stream power index map (Figure 6f) clearly reflect the topography inside the gully channel. These maps, mostly in combination, thus provided a precise delineation of gully thalwegs. The stream power index map has also aided the identification and mapping of certain portions of the gully channel, given the well-expressed slope ridges. The delineated polygon representing the gully channel and lines representing the gully thalwegs are presented on the hillshade map in Figure 6g. In this case, delineation of the gully thalwegs was performed first and it significantly helped in the visualization of the shape and extent of the gully channel. The gully was also previously known, due to its formation near the county road. However, its topography is not visible on DOM 1:5000 (Figure 6h), but indices of erosion processes are marked as alterations in the vegetation type.

The topography of a linear and narrow gully (area of 2185 m^2) formed in the central part of the Vinodol Valley is shown in Figure 7. The overall appearance of the gully channel and thalweg was easily recognized on the hillshade map (Figure 7a). However, the incision point of the gully channel is not clearly expressed on the hillshade map and thus, it was first detected on the slope map and later on the topographic roughness map (highlighted with the white arrow in Figure 7c,d). Changes of slope angle between the gully channel and its surroundings are well expressed in the slope map (Figure 7b), but the continuity of the gully channel shape is more visible on the topographic roughness map (Figure 7c).

On the other hand, the aspect map (Figure 7d) almost entirely overestimates the width of the gully and, in this case, it was considered as ineffective for mapping of the gully channel. The contour line map with 1 m contour interval (Figure 7e) reflects the shape of a small proluvial fan situated at the mouth of the gully channel (pointed with yellow arrows). However, the extent of proluvial desposits could be misinterpreted if only the contour map was visually analyzed. The distal parts of the proluvial fan, highlighted with yellow arrows in Figure 7c, are more clearly recognizable on the topographic roughness map, which thus provided its precise delineation. The stream power index map (Figure 7f) most clearly reflects the linear shape of the gully thalweg, although its features are also well pronounced on the profile curvature map (Figure 7g), and the planform curvature map (Figure 7h). The profile curvature map also aided the mapping of individual portions of the gully channel in its middle and lower parts. The identified gully, shown in Figure 7i, was previously unknown, due to the formation under the forest (Figure 7j), in a nonurbanized area (Figure 7k). Additional analysis of CBM 1:5000 has confirmed that the gully erosion process has affected the forest pathway, as highlighted with red arrows in Figure 7k.

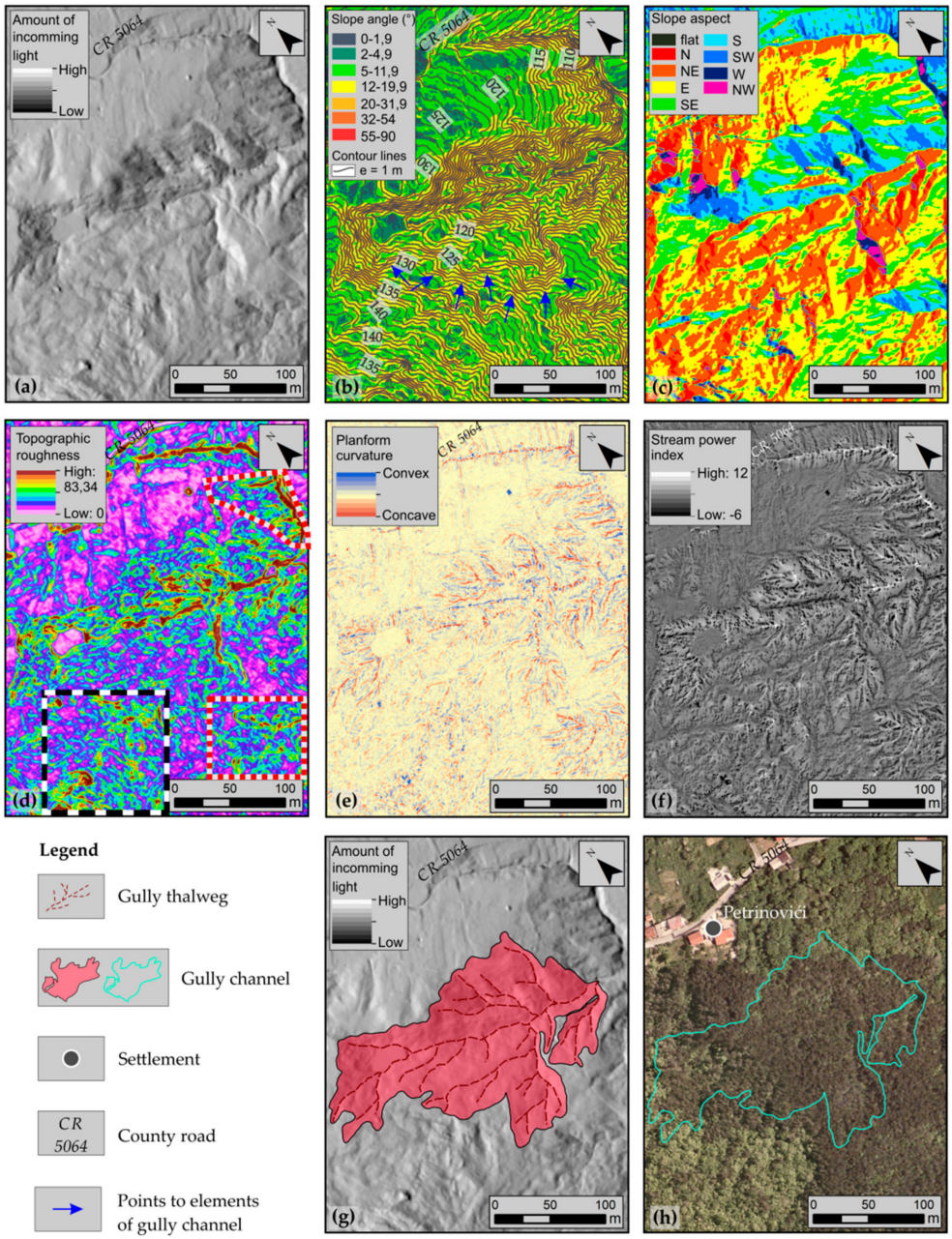

Figure 6. Visualization of topography of a complex gully on HR LiDAR imagery: (**a**) the semi-transparent (50%) hillshade map 45°/45° over the hillshade map 315°/45°; (**b**) the contour line map over the slope map; (**c**) the aspect map; (**d**) the topographic roughness map; (**e**) the planform curvature map; and (**f**) the stream power index map. (**g**) The hillshade map with a delineated polygon representing the gully channel and lines representing the gully thalwegs; and (**h**) the DOM 1:5000 of the interpreted area. In (**d**), the red and white polylines depict the drainage networks and the black and white polyline depicts the debris material formed in the gully surroundings.

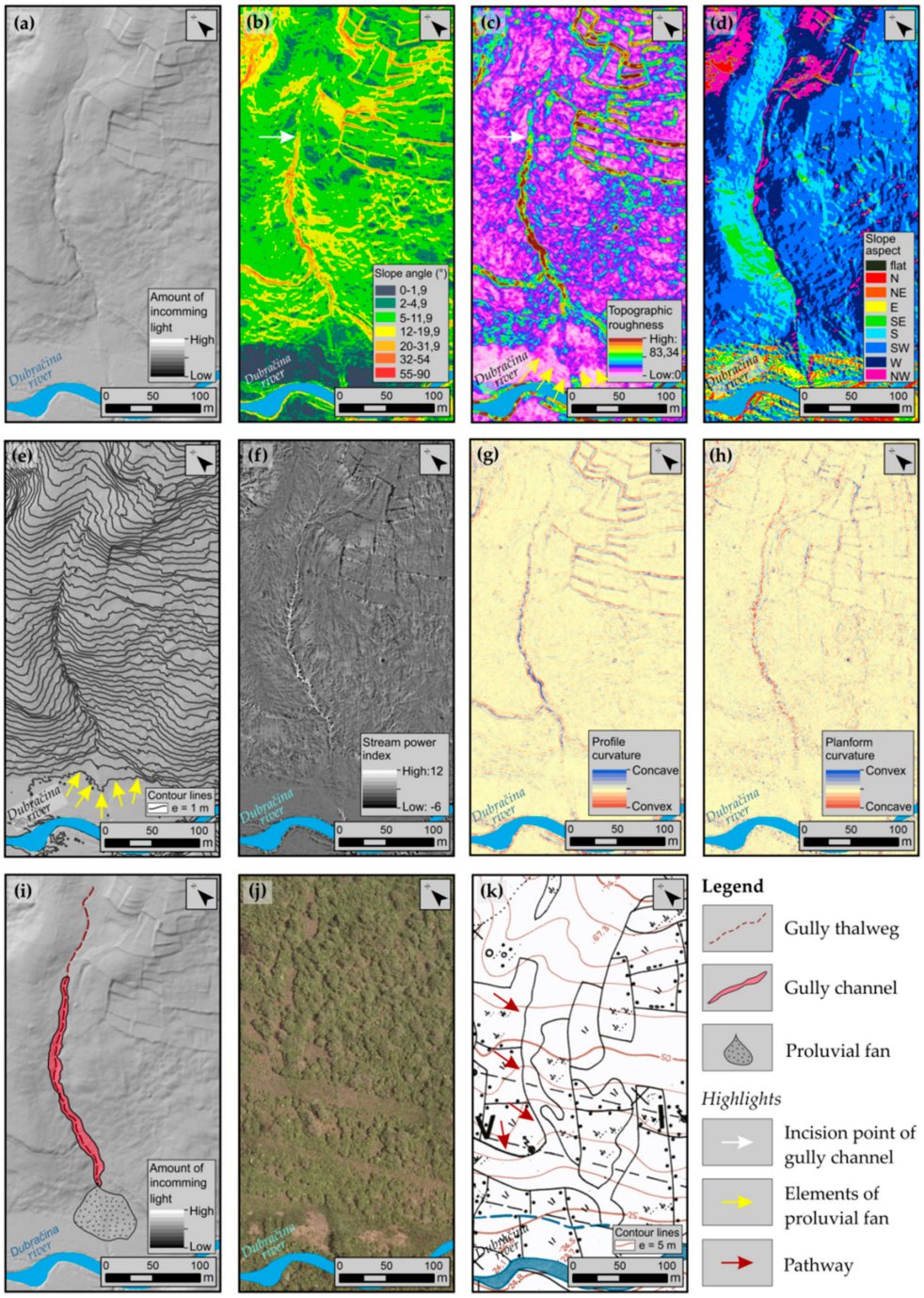

Figure 7. Visualization of topography of a linear and narrow gully on HR LiDAR imagery: (**a**) the semi-transparent (50%) hillshade map 45°/30° over the hillshade map 315°/45°; (**b**) the slope map; (**c**) the topographic roughness map; (**d**) the aspect map; (**e**) the contour line map over the hillshade map; (**f**) the stream power index map; (**g**) the profile curvature map; and (**h**) the planform curvature map. (**i**) The hillshade map with a delineated polygon representing the gully channel and a line representing the gully thalweg. A small proluvial fan was identified at the mouth of the gully channel. (**j**) The DOM 1:5000 and (**k**) the CBM 1:5000 of the interpreted area.

The topography of one of the smallest gullies (area of 1883 m^2) identified on LiDAR imagery is shown in Figure 8. The gully was first recognized in the field, and subsequently on LiDAR maps. It is situated in the northwestern part of the Vinodol Valley in a nonurbanized area. The shape of the gully channel was first recognized on the hillshade map (Figure 8a). Its edges, highlighted with red arrows,

are clearly expressed on the slope map (Figure 8b), the topographic roughness map (Figure 8c), and the profile curvature map (Figure 8d). In this case, an easy recognition of channel was due to the relatively smoothed topography of the surrounding slopes and their almost uniform curvature. The contour line map (Figure 8e) also reflects the shape of the gully channel in its flanks (highlighted with red arrows), but not the accurate shape in its top part (pointed with black arrow). On the other hand, the aspect map (Figure 8f) partially enables recognition of the left channel wall. The contour line map (Figure 8e) also provides recognition of proluvial deposits situated at the mouth of the gully channel. Contours, however, reflect only a general shape of the small proluvial fan (pointed with blue arrows), but not the shape of its distal part (pointed with yellow arrows). Therefore, the texture analysis of proluvial deposits (pointed with blue arrows in Figure 8c) significantly contributed to their mapping. The gully thalweg was not expressed, which was determined based on the analysis of the planform curvature map (Figure 8g) and the stream power index map (Figure 8h). Due to the gentle slope angles and the smooth topography, it is assumed that the gully bottom is covered by proluvial deposits (Figure 8i).

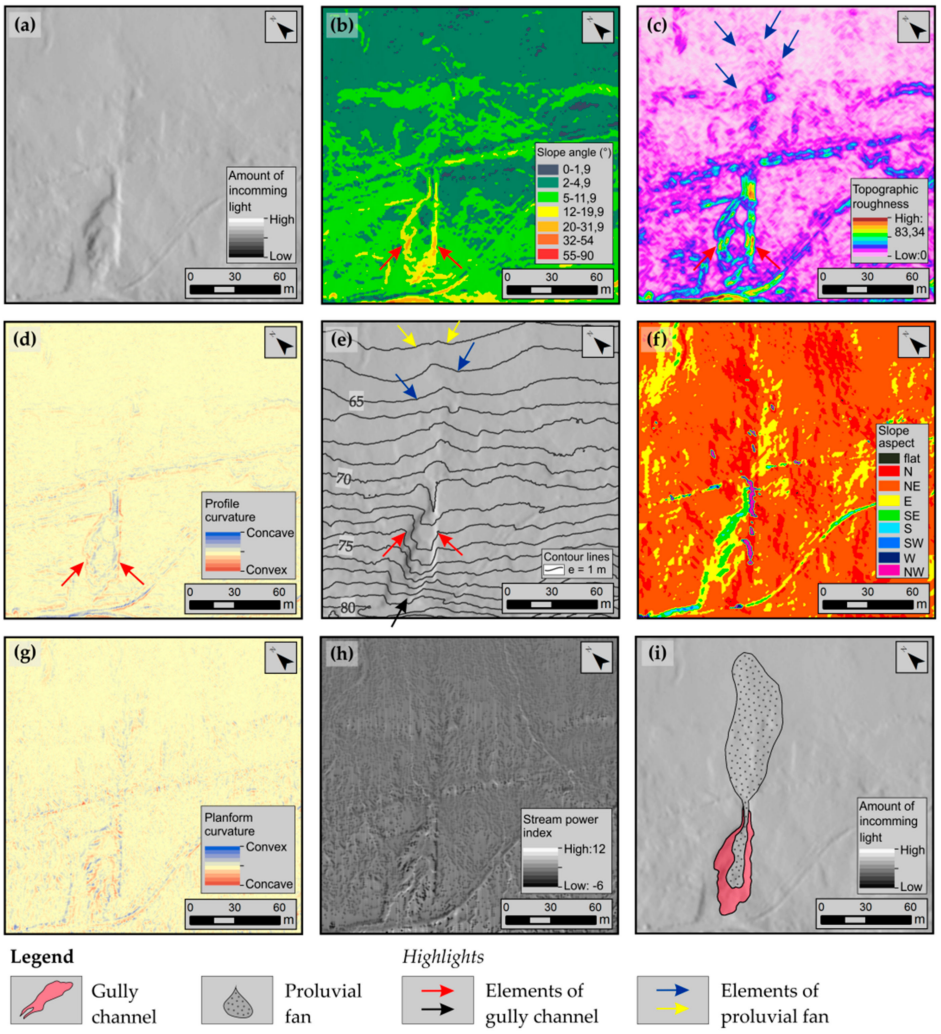

Figure 8. Visualization of topography of a small gully on HR LiDAR imagery: (**a**) the semi-transparent (50%) hillshade map 45°/45° over the hillshade map 315°/45°; (**b**) the slope map; (**c**) the topographic roughness map; (**d**) the profile curvature map; (**e**) the contour line map over the hillshade map; (**f**) the aspect map; (**g**) the planform curvature map; and (**h**) the stream power index map. (**i**) The hillshade map with delineated polygons representing the gully channel and the proluvial fan.

4.2. Identification and Mapping of Combined Erosion Phenomena

Figure 9 presents an example of identification and mapping of the area affected by the combined erosion processes, situated in the central part of the Vinodol Valley. A generally disturbed surface appearance was first recognized on the hillshade map (Figure 9a). A small drainage network was recognized on the stream power index map (Figure 9b) and the planform curvature map (Figure 9c). These recognition features were mainly recognized within the relief concavities surrounding the gully channels. The rough texture of the affected areas (Figure 9d) distinguishes them from the surroundings. However, the recognition features shown in Figure 9a–d were not specific to the surface of all relief concavities in the study area, even though the gullies were formed at their central part and the proluvial and colluvial deposits were accumulated in the toeslope [55]. Thus, the topographic location was considered to be the most relevant recognition feature for identification and mapping of combined erosion phenomena, coupled with the typical pattern representing gullies identified in the central part of relief concavities. A precise delineation of areas considered to be affected by the combined erosion processes was carried out based on the visual analysis of the aspect map (Figure 9e) and the slope map, coupled with the contour line map (Figure 9f), similar to the example shown in Figure 9g.

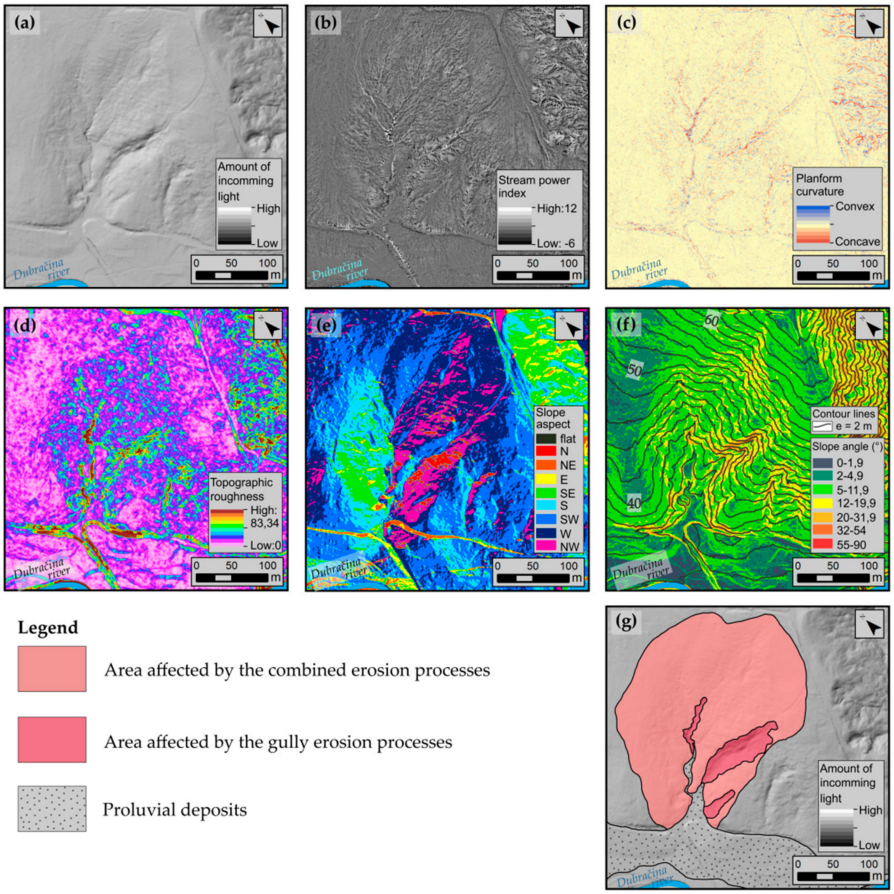

Figure 9. Visualization of topography of area affected by the combined erosion processes on HR LiDAR imagery: (**a**) the semi-transparent (50%) hillshade map 45°/45° over the hillshade map 315°/45°; (**b**) the stream power index map; (**c**) the planform curvature map; (**d**) the topographic roughness map; (**e**) the aspect map; (**f**) the contour line map over the slope map. (**g**) The hillshade map with delineated polygons representing the area affected by the combined erosion processes, the area affected by the gully erosion processes, and the proluvial deposits.

4.3. Identification and Mapping of Sheet Erosion Phenomena

The sheet erosion processes in the study area were first identified in the field. It was found that the sheet erosion predominantly acts on slopes mostly built of eluvial deposits with sporadic flysch outcrops. Since these processes do not form specific morphological features on the affected surface, the direct recognition of sheet erosion on LiDAR maps was not possible. Hence, the first step in mapping of the sheet erosion phenomena was the interpretation of the engineering geological map of the Vinodol Valley [55] to locate areas of eluvial and colluvial deposits (Figure 10a). The assumption that colluvial deposits were formed by the reoccurring sheet erosion processes on the surface of eluvial deposits was proven by determination that the colluvial deposits are located at the foot of the eluvial slopes in almost the entire studied area. The relatively smooth surface topography of eluvial slopes, which can also be considered as indicative for the sheet erosion, was additionally recognized on the topographic roughness map (Figure 10b). In accordance with all presumptions, the mapping of the sheet erosion phenomena was performed indirectly, based on the reinterpretation and transformation of the boundaries of eluvial deposits (Figure 10a) into the polygons representing the areas affected by the sheet erosion processes (Figure 10c).

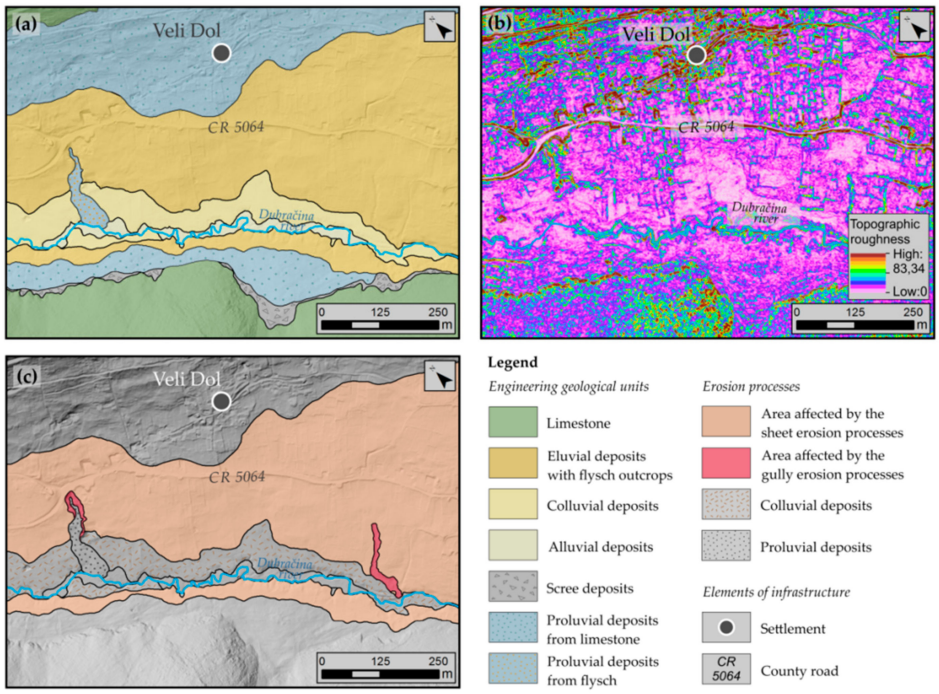

Figure 10. An example of identification and mapping of the sheet erosion processes: (**a**) a detail from the EGM 1:5000 [55]; and (**b**) a visualization of the same area on the topographic roughness map. (**c**) The hillshade map with delineated polygons representing areas affected by the sheet erosion processes and areas affected by the gully erosion.

4.4. Erosion Inventory Map of Vinodol Valley

The erosion inventory map of the Vinodol Valley [55] depicts all past and current soil erosion phenomena identified and mapped based on the detailed visual interpretation of HR LiDAR imagery. The age and the state of activity of the erosion phenomena were not differentiated in this study. The erosion inventory map also shows the spatial distribution of proluvial and colluvial deposits [55], which have been formed by the soil erosion processes. Given the content and the methodology for the preparation, the erosion inventory map of the Vinodol Valley (Figure 11) represents the historical erosion inventory.

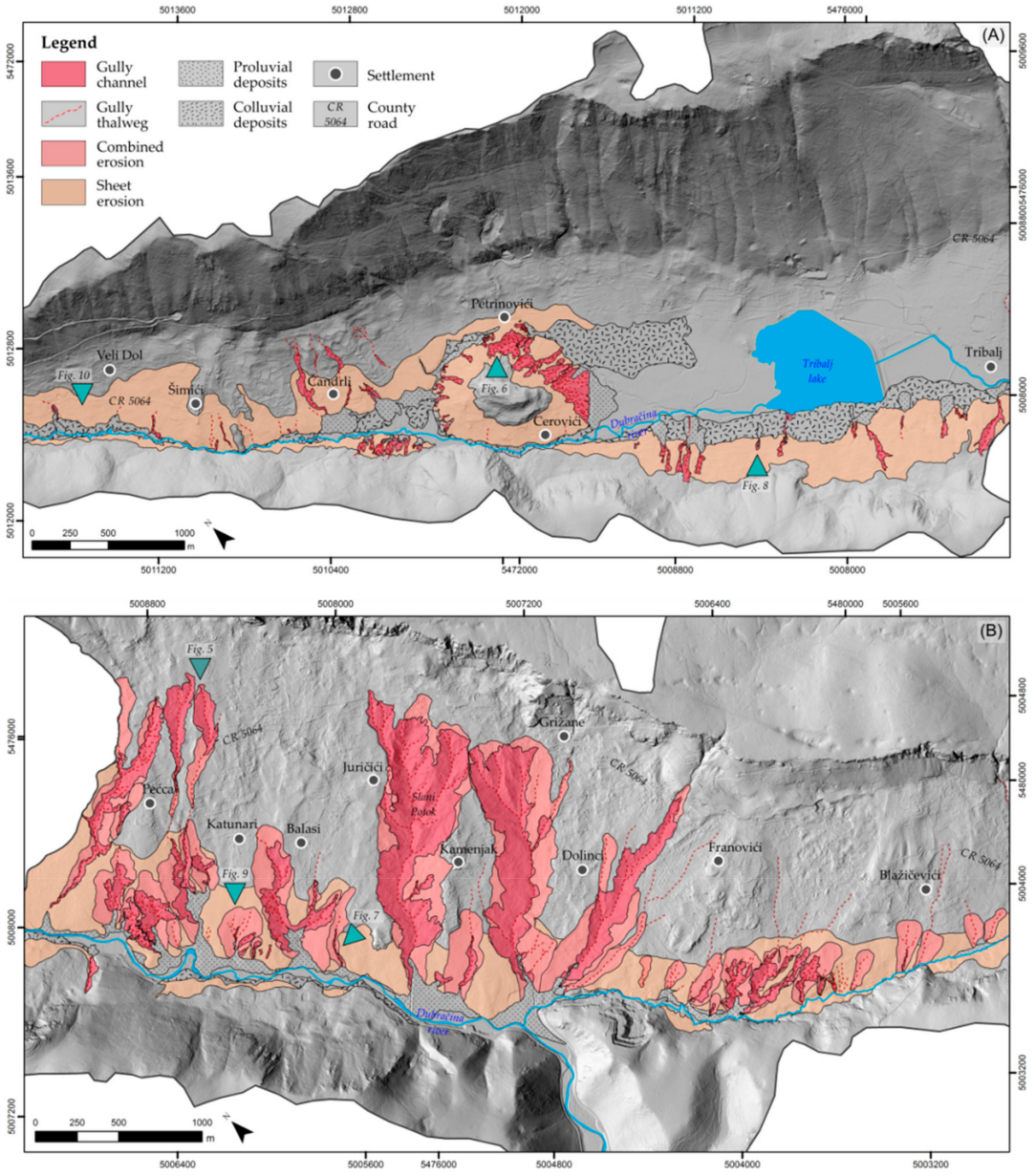

Figure 11. Details from the erosion inventory map of the Vinodol Valley for (**A**) the northwestern part and (**B**) the central part of the valley. Green marks highlight examples of erosion phenomena presented in previous figures.

The topography of 236 gullies in the Vinodol Valley was recognized and mapped on LiDAR imagery [55]. In total, 124 gullies were mapped using polygons and 112 gullies were mapped using lines. The total area of delineated gully channels is 1.89 km^2. The area of the smallest identified gully channel is 95.75 m^2 and the area of the largest identified gully (i.e., Slani Potok) is 47.69 ha. Areas affected by the combined erosion processes were delineated with 53 polygons. Their total area is 2.92 km^2. Areas affected by the sheet erosion processes were delineated with 49 polygons, and their total area is 5.11 km^2. Only the gully and the sheet erosion processes were identified in the northwestern part of the Vinodol Valley (Figure 11a). Most of the gullies are relatively small (areas in range between 95.75 m^2 and 1.75 ha). Significantly larger and morphologically more complex gullies, with areas in range between 317.44 m^2 and 47.69 ha, have formed in the central part of the Vinodol Valley (Figure 11b). Most of them are surrounded by areas affected by the combined erosion processes.

5. Discussion

The visual interpretation of HR LiDAR imagery has shown that for most of identified gullies, the shape of the gully channel and the thalweg were generally recognizable already on the hillshade map. The easiest to identify was the shape of relatively large gully channels with well-preserved topography, such as the gullies shown in Figure 5a, which could be easily distinguished from the morphology of the surrounding slopes. Such topography is characteristic for most of the gullies identified in the central part of the Vinodol Valley (Figure 11b). However, even the small gully channels, which prevail in the northwestern part of the Vinodol Valley (Figure 11a), could have been easily and clearly identified on the hillshade map, especially if there were no other morphological forms or phenomena formed in their surroundings (Figure 8a). On the other hand, it was difficult to fully identify certain gully channels on a hillshade map, even if they were relatively large and complex (Figure 6a). One of the main reasons for this could be the uneven shading of the surface [38,67], because not all parts of the complex gully share a similar aspect (Figure 6c). In this case, however, the reduced effectiveness of the hillshade map in recognizing the full shape of the gully channel was primarily due to the similar surface morphologies of the gully and its surrounding slopes. The effectiveness of the hillshade map was also confirmed to be reduced in recognizing of the incision points of relatively narrow gully channels (Figure 7a). Given all of this, the hillshade map in this study proved to be a powerful aid in the general recognition of the gully phenomena. This was mainly expected, considering that the hillshade map was commonly used as the first map in most of the studies that used a visual interpretation of LiDAR imagery e.g., [21,23,37]. However, it was determined that the topography of the surrounding slopes and the width of the gully channel can considerably limit an accurate identification of the total extent of a gully channel on the hillshade map. For this reason, a precise delineation of a gully channel based on a visual interpretation of the hillshade map is not recommended.

The slope map proved to be the most useful for a precise delineation of gully channels due to the steep topography of channel walls in most of the identified gullies and the well-defined changes of slope angle between the gully channels and the surrounding slopes (Figure 5c, Figure 7b, and Figure 8b). The aspect map was determined to be an effective tool for delineation of almost symmetrical linear gully channels (Figure 5b). However, its effectiveness varied depending on the gully channel width (Figure 7d), and the morphological conditions of the gully surroundings (Figure 6c). The contour line map significantly aided delineation of gully channels, especially of channels with more complex shapes (Figure 6b). Regardless of the shape and topography, the contour line map was generally used in this study for more confident delineation of all gully channels, coupled with the slope map and the aspect map. Even the stream power index map and the profile curvature map, in some cases, proved to be a helpful supplement in delineation of the gully channels (Figures 6f and 8d). The rough surface could also efficiently point to the gully channel extent, but only in conditions of relatively smoothed topography of the surrounding slopes (Figures 7c and 8c). Based on our experience, the topographic roughness map is considered to be a useful tool for recognition of the gully channel given its rough texture, but its effectiveness in this study was generally reduced given the specific surface morphology of the Vinodol Valley (Figure 3), which predominantly reflects also the rough texture. The linear patterns of the planform curvature map and the stream power index map were generally an effective indicator of the extent of the gully drainage network. These maps, mostly coupled, were used for the precise delineation of all the gully thalwegs. The visual analysis of these maps also aided identification and mapping of individual gully channels in areas where several gullies were situated in close proximity (Figure 6e,f).

Unlike the gully erosion, identification of the combined erosion phenomena directly from the LiDAR imagery was partially limited. The main recognition features for identification of the combined erosion phenomena were the topographic location and pattern. All areas delineated as areas affected by the combined erosion processes are located within the relief concavities, with gullies formed in their central parts (Figure 11b). Such a spatial arrangement of gullies was interpreted as a consequence of the running water convergence within the relief concavities [66]. Direct identification of the combined

erosion phenomena on LiDAR maps was possible only sporadically, based on the recognition of generally disturbed slope appearance on the hillshade map (Figure 9a). A relatively small drainage network, which was first identified in the field (Figure 2k–m), was, in places, recognizable on the stream power index map and the planform curvature map (Figure 9b,c). According to adopted criteria, delineation of areas affected by the combined erosion processes was performed after delineation of gullies on the basis of the visual interpretation of the aspect map, slope map, and contour map.

There were the fewest possibilities for identification and mapping of the sheet erosion processes directly from the LiDAR imagery. The first and most important step in identification of the sheet erosion phenomena was the recognition of colluvial deposits, considered as lithologic evidence of the sheet erosion activity. After the analysis of their spatial distribution on the EGM of the Vinodol Valley 1:5000 [55], field checks were carried out. Although field investigations were limited, it was possible to identify the sheet erosion processes active predominantly on the surface of the eluvial deposits ((Figure 2n–p). Thus, the mapping of the sheet erosion processes in the Vinodol Valley was performed indirectly, based on the reinterpretation of spatial distribution of the colluvial and eluvial deposits [55].

The quality assessment of the erosion inventory of the Vinodol Valley can be carried out in comparison with the quality assessment of landslide inventory maps, which depends on the geographical accuracy and thematic certainty of information [14]. According to the criteria for identification, and to the procedure of delineation, the geographical accuracy and thematic level of certainty of the gully erosion phenomena is considered high. The potentially reduced thematic certainty can be related only to very narrow gullies, which were delineated along the pathways, in cases where gully erosion does not occur along the whole delineated line. Areas affected by the combined erosion processes are also characterized by a high level of geographical accuracy. On the other hand, the thematic certainty was potentially reduced because the phenomena were primarily identified based on the recognition of relief concavities, the surfaces of which have not been necessarily affected by the combined erosion processes in the entire studied area. Geographical accuracy of areas affected by the sheet erosion processes was probably reduced due to the lack of topographic signatures specific to these phenomena. Thus, it depends on the geographical accuracy of the eluvial deposits determined during the creation of the EGM of the Vinodol Valley 1:5000 [55]. There was also potentially reduced thematic accuracy with regard to the mapping of the sheet erosion processes, because the erosion does not necessarily act on the surface of all delineated eluvial slopes. Further detailed field investigations are required to improve the quality of these results.

Based on the experience in this study, the preliminary visual interpretation of HR LiDAR imagery is considered to be the most important step in the preparation of an erosion inventory for several reasons. First, this procedure has enabled the determination of significantly different possibilities for identification and mapping of the soil erosion phenomena from the LiDAR imagery already in the earliest phase of investigation. Second, this procedure enables a clear definition of criteria for identification and mapping of the erosion phenomena, whose application during the detailed visual interpretation of LiDAR imagery considerably reduces the consumed time since the investigator knows exactly what he is searching for and on which of the LiDAR maps to look. Finally, the preliminary visual interpretation of HR LiDAR imagery pointed out the importance of the previous knowledge of geological conditions in the studied area, in particular of lithological composition, because materials can unambiguously point to the particular soil erosion process.

Although manual mapping of erosion phenomena was time-consuming, it is considered that the same quality of the results could not be obtained by using the conventional geomorphological mapping methods, given the specific topographic characteristics of the studied area (Figure 3). Therefore, the historical erosion inventory prepared using the proposed mapping procedure is considered satisfactorily complete for future applications, such as for erosion susceptibility analyses or for estimating temporal changes in gully erosion. For that purpose, a digital HR DTM can currently be obtained by LiDAR technique only, especially in the case of an area covered with dense vegetation. However, the possibilities of visual recognition of geomorphological phenomena, and thus the quality

of the mapping results, strongly depend on the spatial resolution of imagery usede.g., [29,73], as well as the subjective experience of an investigator [21]. Even though the impact of different DTM resolutions was not investigated in this study, the 1 m resolution of the LiDAR imagery used here was considered adequate to identify most of the gully phenomena [74]. The necessary further research to improve the proposed procedure is to test different spatial resolutions of LiDAR imagery in identification and mapping of different erosion types, especially combined erosion, which should provide better results using a more optimal DTM resolution. Also, another important issue is the validation of the mapping results, which is often difficult to perform within investigations based on the visual interpretation of HR LiDAR imagery [14], but which could have been efficiently conducted in this study if the ground truth of previously mapped erosion features were available.

6. Conclusions

This paper describes the two-step procedure of identification and mapping of gully erosion, combined erosion, and sheet erosion phenomena in large study area (64.57 km^2) using the visual interpretation of HR LiDAR imagery derived from the 1 m DTM. Eight different LiDAR maps were tested for the potential of the direct and unambiguous identification and mapping of soil erosion, according to the well-established criteria. The results indicate that the applied method has the greatest potential for direct identification and mapping of gully erosion, according to the relatively large number of identified and delineated gullies (236 phenomena, with the total area of 1.89 km^2) that previously have never been studied in detail and mapped. The slope map is being considered as the most useful map for delineation of gully channels, while the planform curvature map and the stream power index map are being considered as the most useful for delineation of gully thalwegs. The visual interpretation of HR LiDAR imagery has also been proven as an appropriate method for mapping of the combined erosion phenomena, according to the precise delineation of 53 polygons (total area of 2.92 km^2) depicting the affected areas around the gully channels. However, the thematic certainty of identified combined erosion phenomena could be reduced in places, considering the fact that the topographic location was one of the main indirect recognition features. A higher spatial resolution of LiDAR DTM, e.g., 0.25 × 0.25 m would potentially provide more reliable results in direct identification and delineation of the combined erosion phenomena, as the surface drainage network could be clearly seen on the planform curvature map and the stream power index map.

On the other hand, the method of visual interpretation of HR LiDAR imagery is not applicable for direct identification and precise delineation of the sheet erosion phenomena due to the lack of specific topographic features formed at the affected surface. Still, the sheet erosion processes can be indirectly recognized on certain LiDAR maps based on the recognition of colluvial deposits accumulated at the foot of the eroded hillslopes. This approach can considerably contribute to the identification of the sheet erosion processes in the field, which is necessary prior to the visual interpretation of HR LiDAR imagery. Subsequent delineation of areas affected by the sheet erosion processes can be carried out only if the spatial distribution of erodible deposits is known.

The results of this study indicate that the visual interpretation of HR LiDAR imagery can be fully applied for preparation of geomorphological historical erosion inventories if the gully erosion processes are the main research subject, and it can almost completely replace field investigations. By contrast, the previous knowledge of lithologic composition and more detailed field checks are required if the sheet erosion processes are among the research subjects. In any case, the high quality of the geomorphological historical erosion inventory maps can be obtained through the visual interpretation of as many different LiDAR maps as possible, and their combinations, according to clearly established criteria already in the earliest phase of the investigation. Furthermore, the method used in this study significantly contributed to the knowledge of type, quantity, spatial distribution, and extent of erosion phenomena in the studied area. Finally, the procedure described in this paper is applicable for identification and mapping of soil erosion processes in all study areas that are characterized by the strong anthropogenic influence on surface morphology, as well as the complex geological conditions,

because these characteristics limit the possibilities of using the automated methods for mapping of erosion given the numerous other traces on the affected surface that are not topographic signatures of geomorphological processes.

Author Contributions: Conceptualization, Petra Đomlija, Željko Arbanas; formal analysis, Petra Đomlija; investigation, Petra Đomlija; methodology, Petra Đomlija and Snježana Mihalić Arbanas; software, Petra Đomlija and Sanja Bernat Gazibara; supervision, Snježana Mihalić Arbanas; visualization, Petra Đomlija; writing—original draft, Petra Đomlija; writing—Review and editing, Sanja Bernat Gazibara, Željko Arbanas and Snježana Mihalić Arbanas.

Funding: This research received no external funding.

Acknowledgments: The results presented herein have been obtained in the frame of the Croatian–Japanese bilateral project Risk Identification and Land-Use Planning for Disaster Mitigation of Landslides and Floods in Croatia, funded by Japan Agency for Science and Technology (JST) and Japan International Cooperation Agency (JICA) through the Science and Technology Research Partnership for Sustainable Development (SATREPS) Program. The authors acknowledge the contribution of three anonymous reviewers that improved the quality of the paper.

Conflicts of Interest: The authors declare no conflict of interest.

References

1. Valentin, C.; Poesen, J.; Yong, L. Gully erosion: Impacts, factors and control. *Catena* **2005**, *63*, 132–153. [CrossRef]
2. Selby, M.J. *Hillslope Materials and Processes*, 2nd ed.; Oxford University Press: New York, NY, USA, 1993; pp. 231–242.
3. Conforti, M.; Aucelli, P.P.C.; Robustelli, G.; Scarciglia, F. Geomorphology and GIS analysis for mapping gully erosion susceptibility in the Turbolo stream catchment (Northern Calabria, Italy). *Nat. Hazards* **2011**, *56*, 881–898. [CrossRef]
4. Soms, J. Development and morphology of gullies in the river Daugava Valley, South-Eastern Latvia. *Landf. Anal.* **2011**, *17*, 183–192.
5. Martínez-Casasnovas, J.A.; Antón-Fernández, C.; Ramos, M.C. Sediment production in large gullies of the Mediterranean area (NE Spain) from high-resolution digital elevation models and geographical information systems analysis. *Earth Surf. Process. Landf.* **2003**, *28*, 443–456. [CrossRef]
6. Kirkby, M.J.; Bull, L.J.; Poesen, J.; Nachtergaele, J.; Vandekerckhove, L. Observed and modelled distributions of channel and gully heads—With examples from SE Spain and Belgium. *Catena* **2003**, *50*, 415–434. [CrossRef]
7. Kakembo, V.; Xanga, W.W.; Rowntree, K. Topographic thresholds in gully development on the hillslopes of communal areas in Ngqushwa Local Municipality, Eastern Cape, South Africa. *Geomorphology* **2009**, *110*, 188–194. [CrossRef]
8. Rahmati, O.; Haghizadeh, A.; Pourghasemi, H.R.; Noormohamadi, F. Gully erosion susceptibility mapping: The role of GIS-based bivariate statistical models and their comparison. *Nat. Hazards* **2016**, *82*, 1231–1258. [CrossRef]
9. Bell, F.G. *Geological Hazards: Their Assessment, Avoidance and Mitigation*, 1st ed.; CRC Press, Taylor & Francis Group; Taylor & Francis Group: London, UK; New York, NY, USA, 1999.
10. Joyce, K.E.; Samsonov, S.V.; Levick, S.R.; Engelbrecht, J.; Belliss, S. Mapping and monitoring geological hazards using optical, LiDAR, and synthetic aperture RADAR image data. *Nat. Hazards* **2014**, *73*, 137–163. [CrossRef]
11. Evans, M.; Lindsay, J. High resolution quantification of gully erosion in upland peatlands at the landscape scale. *Earth Surf. Process. Landf.* **2010**, *35*, 876–886. [CrossRef]
12. Conoscenti, C.; Angileri, S.; Cappadonia, C.; Rotigliano, E.; Agnesi, V.; Märker, M. Gully erosion susceptibility assessment by means of GIS-based logistic regression: A case of Sicily (Italy). *Geomorphology* **2014**, *204*, 399–411. [CrossRef]
13. Van Westen, C.J.; van Asch, T.W.J.; Soeters, R. Landslide hazard and risk zonation—Why is it still so difficult? *Bull. Eng. Geol. Environ.* **2005**, *65*, 167–184. [CrossRef]
14. Guzzetti, F.; Mondini, A.C.; Cardinali, M.; Fiorucci, F.; Santangelo, M.; Chang, K.T. Landslide inventory maps: New tools for an old problem. *Earth-Sci. Rev.* **2012**, *112*, 42–66. [CrossRef]

15. Scaioni, M.; Longoni, L.; Melillo, V.; Papini, M. Remote Sensing for Landslide Investigations: An Overview of Recent Achievements and Perspectives. *Remote Sens.* **2014**, *6*, 9600–9652. [CrossRef]
16. Tarolli, P. High-resolution topography for understanding Earth surface processes: Opportunities and challenges. *Geomorphology* **2014**, *216*, 295–312. [CrossRef]
17. Haugerud, R.A.; Harding, D.J.; Johnson, S.Y.; Harless., J.L.; Weaver, C.S.; Sherrod, B.L. High-resolution lidar topography of the Puget Lowland, Washington—A bonanza for earth science. *GSA Today* **2003**, *13*, 4–10. [CrossRef]
18. Chigira, M.; Duan, F.; Yagi, H.; Furuya, T. Using an airborne laser scanner for the identification of shallow landslides and susceptibility assessment in an area of ignimbrite overlain by permeable pyroclastics. *Landslides* **2004**, *1*, 203–209. [CrossRef]
19. Ardizzone, F.; Cardinali, M.; Galli, M.; Guzzetti, F.; Reichenbach, P. Identification and mapping of recent rainfall-induced landslides using elevation data collected by airborne Lidar. *Nat. Hazards Earth Syst. Sci.* **2007**, *7*, 637–650. [CrossRef]
20. Schulz, W.H. Landslide susceptibility revealed by LIDAR imagery and historical records, Seattle, Washington. *Eng. Geol.* **2007**, *89*, 67–87. [CrossRef]
21. Van Den Eeckhaut, M.; Poesen, J.; Verstraeten, G.; Vanacker, V.; Nyssen, J.; Moeyersons, J.; van Beek, L.P.H.; Vandekerckhove, L. Use of LIDAR-derived images for mapping old landslides under forest. *Earth Surf. Process. Landf.* **2006**, *32*, 754–769. [CrossRef]
22. Amudsen, J.; Johnson, S.; Rousea, K.; Wang, H. Using LiDAR-derived DEM's to Delineate and Characterize Landslides in Northern Kentucky and Hamilton County, Ohio. Available online: www.trishock.com/academic/pdf/lidar_landslides.pdf (accessed on 3 July 2019).
23. Petschko, H.; Bell, R.; Glade, T. Effectiveness of visually analyzing LiDAR DTM derivatives for earth and debris slide inventory mapping for statistical susceptibility modeling. *Landslides* **2016**, *13*, 857–872. [CrossRef]
24. Bernat Gazibara, S.; Krkač, M.; Sečanj, M.; Mihalić Arbanas, S. Identification and Mapping of Shallow Landslides in the City of Zagreb (Croatia) Using the LiDAR–Based Terrain Model. In *Advancing Culture of Living with Landslides, Advances in Landslide Science*; Mikos, M., Tiwari, B., Yin, Y., Sassa, K., Eds.; Springer International Publishing: Cham, Switzerland, 2017; pp. 1093–1100.
25. Wehr, A.; Lohr, U. Airborne laser scanning—An introduction and overview. *ISPRS J. Photogramm. Remote Sens.* **1999**, *54*, 68–82. [CrossRef]
26. Razak, K.A.; Straatsma, M.W.; van Westen, C.J.; Malet, J.-P.; de Jong, S.M. Airborne laser scanning of forested landslides characterization: Terrain model quality and visualization. *Geomorphology* **2011**, *126*, 186–200. [CrossRef]
27. Jaboyedoff, M.; Oppikofer, T.; Abellán, A.; Derron, M.-H.; Loye, A.; Metzger, R.; Pedrazzini, A. Use of LIDAR in landslide investigations: A review. *Nat. Hazards* **2012**, *61*, 5–28. [CrossRef]
28. Smith, M.J.; Rose, J.; Booth, S. Geomorphological mapping of glacial landforms from remotely sensed data: An evaluation of the principal data sources and an assessment of their quality. *Geomorphology* **2006**, *76*, 148–165. [CrossRef]
29. Migon, P.; Kasprzak, M.; Traczyk, A. How high-resolution DEM based on airborne LiDAR helped to reinterpret landforms—Examples from the Sudetes, SW Poland. *Landf. Anal.* **2013**, *22*, 89–101. [CrossRef]
30. Jones, A.F.; Brewer, P.A.; Johnstone, E.; Macklin, M.G. High-resolution interpretative geomorphological mapping of river valley environments using airborne LiDAR data. *Earth Surf. Process. Landf.* **2007**, *32*, 1574–1592. [CrossRef]
31. Seppälä, M.V.J. Lidar-Based Detection and Interpretation of Glaciotectonic Features of the Morainic Topography of Finland. *J. Geol. Res.* **2016**, *2016*, 4292806. [CrossRef]
32. Cavalli, M.; Marchi, L. Characterisation of the surface morphology of an alpine alluvial fan using airborne LiDAR. *Nat. Hazards Earth Syst. Sci.* **2008**, *8*, 323–333. [CrossRef]
33. Notebaert, B.; Verstraeten, G.; Govers, G.; Poesen, J. Qualitative and quantitative applications of LiDAR imagery in fluvial geomorphology. *Earth Surf. Process. Landf.* **2009**, *34*, 217–231. [CrossRef]
34. Sarala, P.; Räisänen, J.; Johansson, P.; Eskola, K.O. Aerial LiDAR analysis in geomorphological mapping and geochronological determination of surficial deposits in the Sodankylä region, northern Finland. *GFF* **2015**, *137*, 293–303. [CrossRef]
35. Abalharth, M.; Hassan, M.A.; Klinkenberg, B.; Leung, V.; McCleary, R. Using LiDAR to characterize logjams in lowland rivers. *Geomorphology* **2015**, *246*, 531–541. [CrossRef]

36. Thorndycraft, V.R.; Cripps, J.E.; Eades, G.L. Digital landscapes of deglaciation: Identifying Late Quaternary glacial lake outburst floods using LiDAR. *Earth Surf. Process. Landf.* **2015**, *41*, 291–307. [CrossRef]
37. Bell, R.; Petschko, H.; Röhrs, M.; Dix, A. Assessment of landslide age, landslide persistence and human impact using airborne laser scanning digital terrain models. *Geogr. Ann. Ser. A Phys. Geogr.* **2012**, *94*, 135–156. [CrossRef]
38. Van Den Eeckhaut, M.; Poesen, J.; Verstraeten, G.; Vanacker, V.; Moeyersons, J.; Nyssen, J.; van Beek, L.P.H. The effectiveness of hillshade maps and expert knowledge in mapping old deep-seated landslides. *Geomorphology* **2005**, *67*, 351–363. [CrossRef]
39. Bernat Gazibara, S.; Krkač, M.; Mihalić Arbanas, S. Verification of historical landslide inventory maps for the Podsljeme area in the City of Zagreb using LiDAR-based landslide inventory. *Rudarsko Geolosko Naftni Zbornik* **2019**, *34*, 45–58.
40. James, L.A.; Watson, D.G.; Hansen, W.F. Using LiDAR data to map gullies and headwater streams under forest canopy: South Carolina, USA. *Catena* **2007**, *71*, 132–144. [CrossRef]
41. Höfle, B.; Griesbaum, L.; Forbriger, M. GIS-Based Detection of Gullies in Terrestrial LiDAR Data of the Cerro Llamoca Peatland (Peru). *Remote Sens.* **2013**, *5*, 5851–5870. [CrossRef]
42. Rijal, S.; Wang, G.; Woodford, P.B.; Howard, H.R.; Hutchinson, J.M.S.; Shawn Hutchinson, J.M.; Hutchinson, S.; Schoof, J.; Oyana, T.J.; Li, R.; et al. Detection of gullies in Fort Riley military installation using LiDAR derived high resolution DEM. *J. Terramechanics* **2018**, *77*, 15–22. [CrossRef]
43. Baruch, A.; Filin, S. Detection of gullies in roughly textured terrain using airborne laser scanning data. *ISPRS J. Photogramm. Remote Sens.* **2011**, *66*, 564–578. [CrossRef]
44. Korzeniowska, K.; Korup, O. Mapping gullies using terrain surface roughness. In Proceedings of the 19th AGILE International Conference on Geographic Information Science (AGILE 2016), Helsinki, Finland, 14–17 June 2016.
45. Casalí, J.; Loizu, J.; Campo, M.A.; De Santisteban, L.M.; Álvarez-Mozos, J. Accuracy of methods for field assessment of rill and ephemeral gully erosion. *Catena* **2006**, *67*, 128–138. [CrossRef]
46. Fadul, H.M.; Salih, A.A.; Ali, I.A.; Inanaga, S. Use of remote sensing to map gully erosion along the Atbara River, Sudan. *Int. J. Appl. Earth Obs. Geoinf.* **1999**, *1*, 175–180. [CrossRef]
47. Daba, S.; Rieger, W.; Strauss, P. Assessment of gully erosion in eastern Ethiopia using photogrammetric techniques. *Catena* **2003**, *50*, 273–291. [CrossRef]
48. Casalí, J.; Giménez, R.; Campo-Bescós, M.A. Gully geometry: What are we measuring? *Soil* **2015**, *1*, 509–513. [CrossRef]
49. Nwankwo, C.; Nwankwoala, H.O. Gully Erosion Susceptibility Mapping in Ikwuano Local Government Area of Abia State usin GIS techniques. *Earth Sci. Malays.* **2018**, *2*, 8–15.
50. Fiorucci, F.; Ardizzone, F.; Rossi, M.; Torri, D. The Use of Stereoscopic Satellite Images to Map Rills and Ephemeral Gullies. *Remote Sens.* **2015**, *7*, 14151–14178. [CrossRef]
51. Wang, R.; Zhang, S.; Pu, L.; Yang, J.; Yang, C.; Chen, J.; Guan, C.; Wang, Q.; Chen, D.; Fu, B.; et al. Gully Erosion Mapping and Monitoring at Multiple Scales Based on Multi-Source Remote Sensing Data of the Sancha River Catchment, Northeast China. *ISPRS Int. J. Geo-Inf.* **2016**, *5*, 200. [CrossRef]
52. Garosi, Y.; Sheklabadi, M.; Pourghasemi, H.R.; Besalatpour, A.A.; Conoscenti, C.; Van Oost, K. Comparison of differences in resolution and sources of controlling factors for gully erosion susceptibility mapping. *Geoderma* **2018**, *330*, 65–78. [CrossRef]
53. Mararakanye, N.; Le Roux, J.J. Gully location mapping at a national scale for South Africa. *S. Afr. Geogr. J.* **2012**, *94*, 208–218. [CrossRef]
54. Blašković, I. Tectonics of part of the Vinodol Valley within the model of the continental crust subduction. *Geol. Croat.* **1999**, *52*, 153–189. [CrossRef]
55. Đomlija, P. Identification and Classification of Landslides and Erosion Phenomena Using the Visual Interpretation of the Vinodol Valley Digital Elevation Model. Ph.D. Thesis, Faculty of Mining, Geology and Petroleum Engineering, University of Zagreb, Zagreb, Croatia, 2018. (In Croatian)
56. Jurak, V.; Slovenec, D.; Mileusnić, M. Excessive flysch erosion-Salty Creek. In *Excursion Guide Book of 3rd Croatian Geological Congress*; Biondić, R., Vlahović, I., Velić, I., Eds.; Croatian Geological Survey: Zagreb, Croatia, 2005; pp. 51–55. (In Croatian)

57. Aljinović, D.; Jurak, V.; Mileusnić, M.; Slovenec, D.; Presečki, F. The origin and composition of flysch deposits as an attribute to the excessive erosion of the Slani Potok Valley ("Salty Creek"), Croatia. *Geol. Croat.* **2010**, *63*, 313–322. [CrossRef]
58. Bernat, S.; Đomlija, P.; Mihalić Arbanas, S. Slope movements and erosion phenomena in the Dubračina River Basin: A geomorphological approach. In *Landslide Flood Hazard Assessment, Proceedings 1st Regional Symposium on Landslides in the Adriatic-Balkan Region*; with 3rd Work. Croat. Proj. Risk Identif. Land-Use Plan; Disaster Mitig, L., Mihalić Arbanas, S., Arbanas, Ž., Eds.; Croatian Landslide Group, Faculty of Mining, Geology and Petroleum Engineering, University of Rijeka, Faculty of Civil engineering, University of Zagreb: Zagreb, Croatia, 2014; pp. 79–84.
59. Rogić, V. Vinodol—Contemporary conditions of the regional zonality relations. *Croat. Geogr. Bull.* **1968**, *30*, 104–125. (In Croatian)
60. Đomlija, P.; Bočić, N.; Mihalić Arbanas, S.; Benac, Č. Identification of geomorphological units and hazardous processes in the Vinodol Valley. In Proceedings of the 2nd Regional Symposium on Landslides in the Adriatic-Balkan Region, Belgrade, Serbia; Abolmasov, B., Marjanović, M., Đurić, U., Eds.; Faculty of Mining and Geology, University of Belgrade: Belgrade, Serbia, 2017; pp. 109–116.
61. Zaninović, K.; Gajić-Čapka, M.; Perčec Tadić, M.; Vučetić, M.; Milković, J.; Bajić, A.; Cindrić, K.; Cvitan, L.; Katušin, Z.; Kaučić, D.; et al. *Climate atlas of Croatia 1961-1990, 1971-2000*; Croatian Meteorological and Hydrological Service: Zagreb, Croatia, 2008. (In Croatian)
62. Croatian Agency for Environment and Nature (CAEN). CORINE Land Cover Croatia. Land Use Map 1:100,000. 2008. Available online: http://corine.azo.hr/corine (accessed on 10 May 2019).
63. Đomlija, P.; Bernat, S.; Arbanas Mihalić, S.; Benac, Č. Landslide Inventory in the Area of Dubračina River Basin (Croatia). In *Landslide Science for a Safer Geoenvironment, Vol. 2, Methods of Landslide Studies*; Sassa, K., Canuti, P., Yin, Y., Eds.; Springer International Publishing: Cham, Switzerland, 2014; pp. 837–842. [CrossRef]
64. Mileusnić, M.; Slovenec, D.; Jurak, V. *Thenardite Efflorescence Indicating Cause of the Excessive Flysch Erosion, Slani Potok, Croatia*; Acta Mineralogica-Petrographica, Abstract Series; Nemeth, T., Terbocs, A., Eds.; Department of Mineralogy, Geochemistry and Petrology, University of Szeged: Szeged, Hungary, 2004; p. 75. Available online: http://acta.bibl.u-szeged.hu/31620/1/mineralogica_as_004_075.pdf (accessed on 1 October 2019).
65. Benac, Č.; Jurak, V.; Oštrić, M.; Holjević, D.; Petrović, G. Excessive erosion phenomena in the Salty Creek Catchment (Vinodol Valley). In *Abstract Book of the 3rd Croatian Geological Congress*; Velić, I., Vlahović, I., Biondić, R., Eds.; Croatian Geological Survey: Zagreb, Croatia, 2005; pp. 173–174.
66. Toy, T.J.; Foster, G.R.; Renard, K.G. *Soil Erosion: Processes, Prediction, Measurement, and Control*, 1st ed.; John Wiley and Sons: New York, NY, USA, 2002.
67. Schulz, W.H. Landslides Mapped Using LIDAR Imagery, Seattle, Washington. United States Geological Survey, Open-File Report 2004-1396. Available online: https://pubs.usgs.gov/of/2004/1396 (accessed on 3 July 2019). [CrossRef]
68. International Geographical Union (IGU), Commision on Applied Geomorphology, Subcommission on geomorphological mapping. The Unified Key to the Detailed Geomorphological Map of the World 1:25000–1:50000. In *Problems of the Detailed Geomorphological Map, Part I.*; Project of the Unified Key to the Detailed Geomorphological Map of the World, Part II; Gellert, J., Jolly, F., Eds.; Folia geographica, Series Geographica Physica: Krakow, Poland, 1968.
69. Ruszkiczay-Rüdiger, Z.; Fodor, L.; Horváth, E.; Telbisz, T. Discrimination of fluvial, eolian and neotectonic features in a low hilly landscape: A DEM-based morphotectonic analysis in the Central Pannonian Basin, Hungary. *Geomorphology* **2009**, *104*, 203–217. [CrossRef]
70. Popit, T.; Verbovšek, T. Analysis of surface roughness in the Sveta Magdalena paleo-landslide in the Rebrnice area. *RMZ-Mater. Geoenviron.* **2013**, *60*, 197–204.
71. Reuter, H.I.; Hengl, T.; Gessler, P.P. Preparation of DEMs for Geomorphometric Analysis. In *Geomorphometry—Concepts, Software, Applications. Developments in Soil Science*; Hengl, T., Reuter, H.I., Eds.; Elsevier: Amsterdam, The Netherlands, 2009; Volume 3, pp. 87–120. [CrossRef]
72. Moore, I.D.; Grayson, R.B.; Ladson, A.R. Digital terrain modelling: A review of hydrological, geomorphological, and biological applications. *Hydrol. Process.* **1991**, *5*, 3–30. [CrossRef]

73. Fiorucci, F.; Cardinali, M.; Carlà, R.; Rossi, M.; Mondini, A.C.; Santurri, L.; Ardizzone, F.; Guzzetti, F. Seasonal landslide mapping and estimation of landslide mobilization rates using aerial and satellite images. *Geomorphology* **2011**, *129*, 59–70. [CrossRef]
74. Dai, W.; Yang, X.; Na, J.; Li, J.; Brus, D.; Xiong, L.; Tang, G. Effects of DEM resolution on the accuracy of gully maps in loess hilly areas. *Catena* **2019**, *177*, 114–125. [CrossRef]